EXPERIMENTAL EVALUATION OF NOVEL COMPOSITES FOR USE IN TRANSPORT OF EXPLOSIVE MATERIALS

Carl-Ernst Rousseau, Alex Bogdanovich, Arun Shukla
Shrikrishna Badiger, and Jim Leblanc
University of Rhode Island

April 2005

URITC PROJECT NO. 000057

PREPARED FOR

UNIVERSITY OF RHODE ISLAND
TRANSPORTATION CENTER

1. Report No	2. Government Accession No.	3. Recipient's Catalog No.
URITC FY 03-01	N/A	N/A

4. Title and Subtitle	5. Report Date
Experimental Evaluation of Novel Composites for Use in Transport of Explosive Materials	April 2005
	6. Performing Organization Code N/A

7. Authors(s)	8. Performing Organization Report No.
Carl-Ernst Rousseau, Alex Bogdanovich, Arun Shukla Shrikrishna Badiger, and Jim Leblanc	N/A

9. Performing Organization Name and Address	10. Work Unit No. (TRAIS)
University of Rhode Island, Dept. of Mechanical Engineering, 222-B Wales Hall, Kingston, RI 02881 (401) 874- 2542 rousseau@egr.uri.edu	N/A
	11. Contract or Grant No. URI 500230400000000057
	13. Type of Report and Period Covered Final

12. Sponsoring Agency Name and Address	14. Sponsoring Agency Code
University of Rhode Island Transportation Center Carlotti Administration Building, 75 Lower College Road Kingston, RI 02881	A study conducted in cooperation with U.S. DOT

15. Supplementary Notes
N/A

16. Abstract

This report describes research activities undertaken to determine the blast resistance of novel materials proposed as an alternative to materials in current use in the transportation industry. The focus of the current study is a 3D woven S-2 glass fabric manufactured by 3TEX, Inc. The project was first initiated with the design and construction of a shock tube facility. The designed shock tube is capable of producing blasts in excess of the energy output of black powder. In addition, the relative performance of three-dimensional panels from 3TEX, Inc. was initiated. Post-mortem evaluations performed on those panels indicate that the use of superimposed lighter weight plies is preferable to using heavy weight multiple plies, and by far exceeds the performance of heavy single plies of the same thickness.

17. Key Words	18. Distribution Statement
Blast loading, wave propagation, truck panels, shock tube	No restrictions. This document is available to the Public through the URI Transportation Center, Carlotti Administration Building, 75 Lower College Rd., Kingston, RI 02881

19. Security Classif. (of this report)	20. Security Classif. (of this page)	21. No. of Pages	22. Price
Unclassified	Unclassified	46	N/A

Form DOT F 1700.7 (8-72) Reproduction of completed page authorized (art. 5/94)

TABLE OF CONTENTS

		Page
	ABSTRACT	**1**
1.	**INTRODUCTION**	**2**
2.	**BLAST LOADING MECHANISM**	**2**
	2.1 Introduction	**2**
	2.2 Theory of the Shock Tube	**3**
	2.3 Design and Fabrication of the Shock Tube	**13**
3.	**DESIGN AND FABRICATION OF PROPOSED MATERIAL**	**20**
4.	**VERIFICATION OF THE NUMERICAL SCHEME**	**24**
	4.1 Introduction	**24**
	4.2 Formulation of Boundary Conditions	**26**
	4.3 Verification of Computational Meshes	**27**
5.	**BLAST LOADING EXPERIMENTS**	**31**
	5.1 Materials Available for Testing	**31**
	5.2 Experiments	**33**
	5.3 Post-Mortem Evaluation	**35**
6.	**SUMMARY**	**37**
7.	**ACKNOWLEDGEMENT**	**38**
8.	**REFERENCES**	**39**

LIST OF FIGURES

Figure 1. Spreading of compressive disturbances produced in a fluid moving at constant (a) subsonic, (b) sonic and (c) supersonic speeds. 4
Figure 2. Simple shock tube with both ends closed. 5
Figure 3. Wave (*x*-*t*) diagram in a simple shock tube closed at both ends. 6
Figure 4. Sketch of a shock wave. Velocities indicated at upstream and downstream of the shock wave are with respect to shock wave. 7
Figure 5. Motion of waves and gases in double diaphragm shock. 11
Figure 6. Schematic of double diaphragm shock tube with convergent section. 14
Figure 7. Comparison of different shock tube configurations. Legend: Single Diaphragm (SD), Double Diaphragm (DD), Single Diaphragm with Convergent section (SDC) and Double Diaphragm with Convergent section (DDC). 15
Figure 8. Driver section. 16
Figure 9. Intermediate 1, Intermediate 2, Convergent, Driven section and dump tank. 17
Figure 10. Burst aluminum diaphragm. 17
Figure 11. Assembled Shock Tube. 18
Figure 12. Variation of wave velocity (a), shock pressure (b), and reflected pressure (c) as a function of shock tube burst pressure. 19
Figure 13. In-scale computer-generated images of "93oz" 3-D woven fabric (left) and its composite (right) elements. 22
Figure 14. Experimental (left) and computer-generated (right) cross-sectional images of "93oz" 3-D woven fabric composite. 23
Figure 15. Unit Cell construction of "93oz" 3-D woven fabric composite. 23
Figure 16. Surface photos of "93oz" 3-D woven fabric (left) and its composite (right). 24
Figure 17. A typical Pressure-Time variation associated with an incident blast pulse. The pulse peak value and its duration are taken arbitrarily here; for any specific blast loading case they have to be related to the explosive characteristics. 26
Figure 18. Schematic of a multi-layer panel exposed to uniformly distributed pressure pulse, and boundary conditions imposed along the side surfaces. 27
Figure 19. One-quarter of the panel solved in present analysis. 27
Figure 20. Discretization mesh 28
Figure 21. Numerical results for Panel #1. 30
Figure 22. Photograph of specimen prior to testing. 31
Figure 23. Double-ply cut-out. 33
Figure 24. Surface damage to plate subjected to 600 psi input pressure. 34
Figure 25. Extensive fiber damage in plate subjected to 850 psi input pressure. 34
Figure 26. Compression apparatus. 35
Figure 27. Two forms of failures obtained during compression testing: a) fiber crushing (190 oz) and b) fiber kinking (93 oz). 36
Figure 28. Microscopic examination of a) crushed and b) kinked fibers 37

LIST OF TABLES

Table 1. Dimensions of the Shock Tube Sections 14
Table 2. 3D Weave materials procured for testing 32
Table 3. Result of compressive testing 36

ABSTRACT

This report describes research activities undertaken to determine the blast resistance of novel materials proposed as an alternative to materials in current use in the transportation industry. The focus of the current study is a 3D woven S-2 glass fabric manufactured by 3TEX, Inc. The project was first initiated with the design and construction of a shock tube facility. The designed shock tube is capable of producing blasts in excess of the energy output of black powder. In addition, the relative performance of three-dimensional panels from 3TEX, Inc. was initiated. Post-mortem evaluations performed on those panels indicate that the use of superimposed lighter weight plies is preferable to using heavy weight multiple plies, and by far exceeds the performance of heavy single plies of the same thickness.

1. INTRODUCTION

This report describes research activities undertaken to determine the blast resistance of novel materials proposed as an alternative to materials in current use in the transportation industry. The focus of the current study is a 3D woven S-2 glass fabric manufactured by 3TEX, Inc. of Cary, North Carolina. Prior to expanding experimental efforts, the majority of the work pertaining to this stage of the project focused on the development of a device capable of generating blasts similar to those produced by explosives. This device, called the shock tube, is capable of producing blasts having a magnitude in the range of that produced by a concentration of 2¾ g/cm^3 of black powder. Further redesign could yield far greater explosive output. The current design is used to generate repeated loading on several grades of the three-dimensional composite.

Section 2 of this report presents the steps taken in designing, building, and calibrating the shock tube. Section 3 details the structure of the three-dimensional woven material. The next section introduces the concurrent development of the finite element code undertaken by 3TEX, Inc. to be used in numerical simulations of the experiments. Finally, Section 5 presents the results of the experiments conducted during the current stage of the project.

2. BLAST LOADING MECHANISM

2.1 Introduction

In recent years, interest in the dynamic response of materials to blast loadings has been renewed [1 - 4]. Most researchers engaging into that field have adopted the use of explosives to produce propagating shock waves which then impinge violently upon a specimen with a spherical wave front. The lack of uniformity of the latter is difficult to model, and thus constitutes an undesirable characteristic. In addition, explosives are difficult to control, thereby

raising safety issues. In addition their loading/strain rates cannot be altered. The first problem can be tackled by using sheets of explosive mounted on or near the test specimen [4, 5], or by keeping the explosive at sufficient distance from the test specimen, allow for the creation of more uniform or planar wave fronts [6 - 9]. Shock tubes can also help overcome some of these drawbacks. For example, controlling the blast level translates into the routine matter of merely varying the input pressure. More importantly, pressure and velocity signature produced by a shock tube are identical to those of explosives. However, the relative difficulty in altering the loading/strain rate still constitutes a challenge.

The mechanism of shock tubes was first proposed by Vieille, in 1899, [10, 11] who demonstrated that shock waves could propagate down a tube with a velocity greater than that of sound when a thin diaphragm, separating two fluids at different pressure levels, ruptures. Interest in the subject remained stagnant for several decades, before systematic investigation of waves traveling in the shock tube were reinitiated. Shock tubes have since become an indispensable tool for the study of compressible fluid flow. Its potential as a loading device was realized much later when plastic and aluminum specimens were first subjected to shock [12, 13]. Examples of new materials testing using shock tube loading abounds in the literature [14 - 18].

Having enumerated the advantages of using shock tubes as loading devices, the following section will proceed to explain the processes used to design, fabricate and calibrate the current shock tube facility for use in the study of the dynamic response of materials.

2.2 Theory of the Shock Tube

Prior to discussing the shock tube, it is essential to have a thorough understanding of the notions of shock mechanisms. These concepts are introduced in the following paragraphs.

Consider a semi-infinite wedge of infinitesimal angle located along the line of attack of a uniformly moving fluid. With the fluid as the reference frame, the wedge appears to be moving from left to right at constant speed V, as shown in the Fig. 1. The disturbances in the fluid, produced by the wedge, extend radially at the speed of sound, a, in the fluid medium. The wedge is initially at location "0". Following a time interval Δt the wedge has moved to location "1", traveling a distance $\Delta x = V \cdot \Delta t$, while compressive disturbances originated at "0" have traveled a distance $\Delta x' = a \cdot \Delta t$. At successive increments of the time interval, Δt, the wedge sequentially moves to points "2", "3", and "4".

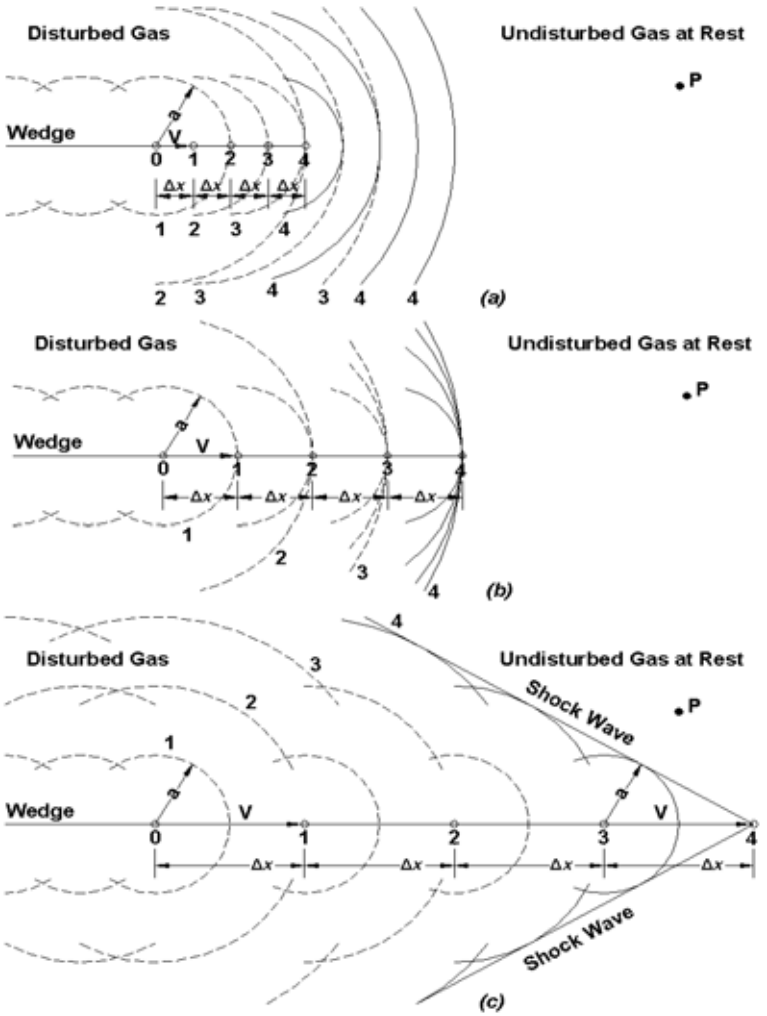

Figure 1. Spreading of compressive disturbances produced in a fluid moving at constant (a) subsonic, (b) sonic and (c) supersonic speeds.

Fluid flow velocity is generally characterized by the Mach number of the flow, described as: $M = \frac{V}{a}$. If $M < 1$ ($V < a$) the flow is "subsonic". When the flow relative to the wedge is subsonic, the infinitesimal disturbances produced by the wedge surfaces in the fluid surround the wedge and spread over the space. Sonic flow occurs when $M = 1$ ($V = a$). In that case, the

infinitesimal disturbances produced in the fluid tend to form a plane front that separates the undisturbed from the disturbed fluid. When $M > 1$ ($V > a$) the flow is supersonic, and the disturbances produced in the fluid are overtaken by the wedge. The fronts of these disturbances form two inclined-plane surfaces, located on either side of the elementary wedge. The area enclosed by these two surfaces is commonly known as the Mach cone. It delineates the boundary outside which the fluid is undisturbed. The shock wave, also know as Mach wave or shock front, is a thin viscous region, across which there is a sudden change in fluid pressure, density, and temperature.

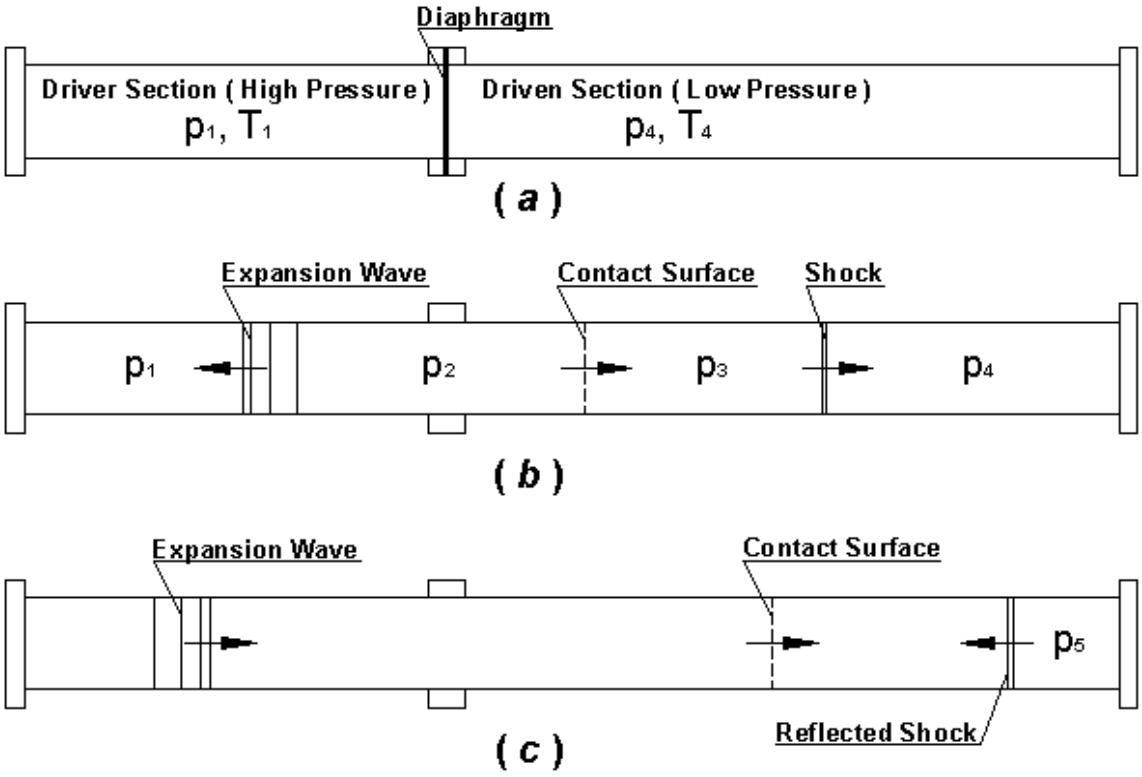

Figure 2. Simple shock tube with both ends closed.

The principles of a shock having been introduced, the physical nature of a shock tube is now presented. A shock tube consists of an enclosed cylinder parted into two sections by a gas-tight diaphragm. A pressure difference is applied to the diaphragm, as shown in Fig. 2, causing

it to rupture. As a result, compression waves steepen rapidly into a shock wave and speed into the driven section while an expansion (rarefaction) wave propagates into the driver section. A contact surface, traveling behind the shock wave, separates the driving from the driven gas. Across this surface velocity and pressure are equal but temperature and density may not be. As the shock front enters region 4, it raises pressure and temperature to higher values denoted by subscript 3. When the shock wave arrives at the boundary, it reflects, further raising pressure and temperature. This condition is denoted by subscript 5.

The motion of the gas and the waves within the shock tube is customarily represented by the *x–t* diagram shown in Figure 3. The origin of the *x–t* diagram is at the location of the diaphragm. Time t initiates at the instant of diaphragm burst. The wave pattern consists of a shock wave propagating into the driven gas which is initially at rest (region 4). The state of the gas after passage of the shock wave (region 3) is one of uniform pressure and uniform fluid velocity. The figure also shows an expansion wave traveling back into driver section (region 1). The region between the tail of the expansion wave and the

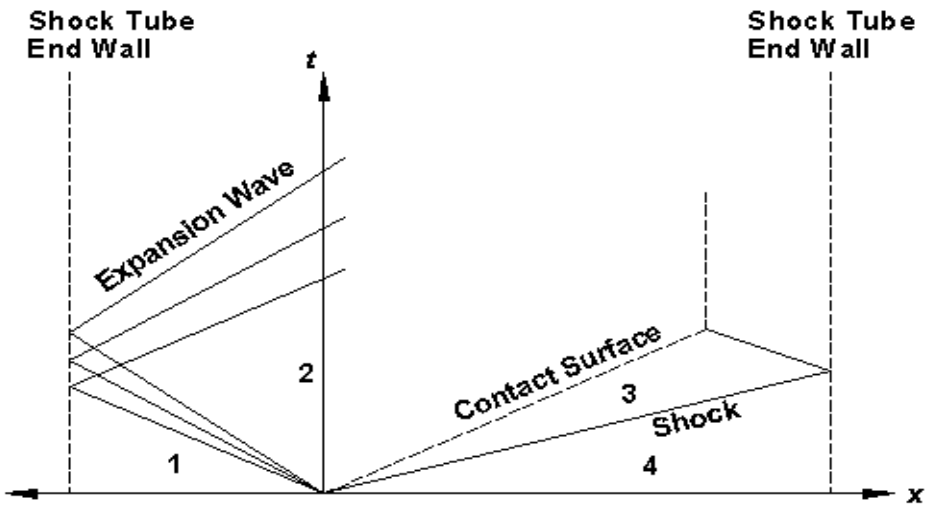

Figure 3. Wave (*x-t*) diagram in a simple shock tube closed at both ends.

contact surface is denoted by 2. The speed of the shock front is a function of (p_1 / p_4), the sound speed of the medium, and ratio of specific heat of the gases in driver and driven sections. The contact surface follows the shock front at a speed lower than the shock speed, whereas the front of the expansion wave travels back at the speed of sound in the driver gas.

Development of Shock Equations

Consider a propagating normal shock wave, as shown in Fig. 4. Region 1 is the upstream of the shock and region 2 is a separate uniform flow downstream of the shock. The pressure, density, temperature, Mach number and velocity in region 1 are p_1, ρ_1, T_1, M_1, u_1, respectively. The corresponding variables in region 2 are denoted by p_2, ρ_2, T_2, M_2 and u_2. Let the flow properties upstream of the shock wave be known, whereas the flow properties downstream of the shock wave are to be calculated. At a particular instant in time, the shock wave is inside the control volume *abcd*. Further, let the cross-section of the area delimited by the boundary be *A*. It is assumed that the flow is steady state and adiabatic, and that there are neither viscous nor body forces affecting the area of interest.

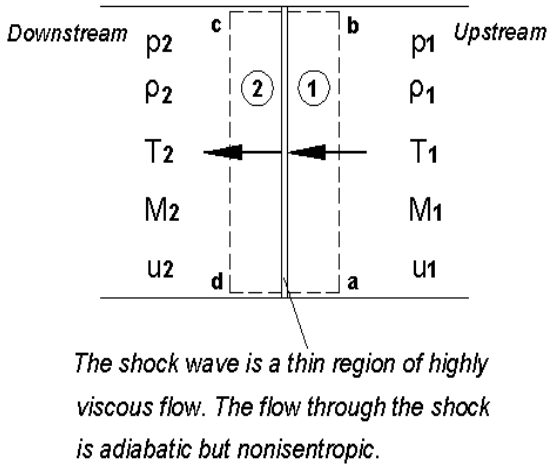

Figure 4. Sketch of a shock wave. Velocities indicated at upstream and downstream of the shock wave are with respect to shock wave.

Applying the conservations of mass, momentum, and energy relations:

$$\rho_1 u_1 = \rho_2 u_2 , \tag{1}$$

$$p_1 + \rho_1 u_1^2 = p_2 + \rho_2 u_2^2 , \tag{2}$$

$$h_1 + \frac{u_1^2}{2} = h_2 + \frac{u_2^2}{2}, \tag{3}$$

results in an underdetermined system of equations, which can be solved only by recalling the equations for enthalpy and the equation of state of Ideal Gases:

$$h_2 = C_P T_2, \tag{4}$$

$$p_2 = \rho_2 R T_2. \tag{5}$$

Variables h, C_p, and R are enthalpy, specific heat, and gas constant, respectively. One set of solutions as derived by Anderson [19] is presented below:

$$\frac{\rho_2}{\rho_1} = \frac{u_1}{u_2} = \frac{(\gamma+1)M_1^2}{2+(\gamma-1)M_1^2}, \tag{6}$$

$$\frac{p_2}{p_1} = 1 + \frac{2\gamma}{\gamma+1}\left(M_1^2 - 1\right), \tag{7}$$

$$\frac{T_2}{T_1} = \frac{h_2}{h_1} = \left[1 + \frac{2\gamma}{\gamma+1}\left(M_1^2 - 1\right)\right]\left[\frac{(\gamma+1)M_1^2}{2+(\gamma-1)M_1^2}\right], \tag{8}$$

where γ is the ratio of specific heats, $M_1 = \frac{u_1}{a_1}$ is the Mach number of the fluid upstream and $a_1 = \sqrt{\gamma R T_1}$ is the speed of sound in the upstream region.

Single Diaphragm Shock Tube

A single diaphragm shock tube is the simplest configuration used for generating normal shock wave. The single diaphragm shock tube with both ends closed was described earlier. Properties downstream of the shock wave can be found if the mach number of the shock front, and upstream properties are known. It is pivotal to find the speed of the shock front in terms of the known variables, p_1, T_1, γ_1, p_4, T_4, γ_4.

To facilitate development of proper equations, use must be made of a shock reference coordinate system, where the shock front is considered stationary. Initial fluid velocities in both driver and driven sections are zero. The shock front travels at speed u_s down the driven section while the expansion front travels back at a_1, the speed of sound in the driver section. Also, the following relation is defined: $u_3' = u_s - u_3$ and $u_4 = u_s - u_4'$, where the primed variable indicate the global motion of the fluid, while the un-primed represent the motion in the stationary coordinate of the traveling shock. Equations (6), (7), and (8) can be applied to the moving shock front, when the shock reference coordinate system is used, yielding appropriate relations between the parameters of regions 3 and 4.

A different approach must be used to obtain valid relations across the expansion wave. The pressure ratio relating the regions 1 and 2 is given by:

$$\frac{p_1}{p_2} = \left(\frac{a_1}{a_2} \right)^{\frac{2\gamma_1}{\gamma_1 - 1}}. \tag{9}$$

Assuming the non-steady expansion to be isentropic, the Riemann variable $\frac{2a}{\gamma - 1} + u$ is constant. Thus, equating that variable across the boundary, and recalling that the gas in the driver section is at rest, the following relation is obtained:

$$a_2 = a_1 - \left(\frac{\gamma_1 - 1}{2} \right) u_2'. \tag{10}$$

Regions 2 and 3 are separated by an entropy discontinuity at their contact surface that travels with the velocity of gas in region 3. On both sides of the contact surface, velocity and pressure are constant. Hence, Eq. (9) can be rewritten as:

$$\frac{p_1}{p_3} = \left(\frac{a_1}{a_1 - \frac{1}{2}(\gamma_1 - 1)u_3'} \right)^{\frac{2\gamma_1}{\gamma_1 - 1}} . \tag{11}$$

The variable $u_3' = u_s - u_3$

Combining Eq's (7) (at the interface between regions 3 and 4) and (11) the following equation relates the conditions between the driver and the driven sections:

$$\frac{p_1}{p_4} = \left(1 + \frac{2\gamma_4}{\gamma_4 + 1}\left(M_4^2 - 1\right) \right) \left(\frac{a_1}{a_1 - \frac{1}{2}(\gamma_1 - 1)u_3'} \right)^{\frac{2\gamma_1}{\gamma_1 - 1}} . \tag{12}$$

From Eq.(6) the induced velocity behind the shock wave can be found,

$$u_3' = \frac{2u_s}{\gamma_4 + 1}\left(\frac{M_4^2 - 1}{M_4^2} \right) = \frac{2a_4}{\gamma_4 + 1}\left(M_4 - \frac{1}{M_4} \right), \tag{13}$$

then introduced into relation (12) to obtain a relation solely in terms of the Mach number:

$$\frac{p_1}{p_4} = \left(1 + \frac{2\gamma_4}{\gamma_4 + 1}\left(M_4^2 - 1\right) \right) \left(\frac{1}{1 - \left\{ \frac{(\gamma_1 - 1)a_4}{(\gamma_4 + 1)a_1} \right\} \left(M_4 - \frac{1}{M_4} \right)} \right)^{\frac{2\gamma_1}{\gamma_1 - 1}} . \tag{14}$$

As expected, the relation predicts an increase in the Mach number of the shock with increasing driver to driven gas pressure ratio.

Double Diaphragm Shock Tube

A schematic representation of a double diaphragm shock tube [20, 21] is shown in Figure 5. It consists of a driver, an intermediate, and a driven section denoted here by subscripts "1", "4", and "8", respectively. Known initial conditions are indicated in the figure. Following the rupture of the first diaphragm and formation of the shock wave, the latter reflects back from diaphragm 2, raising the pressure and the temperature of the already shocked gas (state 3) to a

state denoted by subscript 5. If diaphragm 2 is ruptured because of the ambient conditions of the fluid at state 5, the shock wave the travels forward into the driven section. A contact surface associated with the burst of the diaphragm follows the shock wave while a rarefaction wave travels back towards the intermediate section.

The interaction between the reflected shock wave from the diaphragm 2, the contact surface traveling into the intermediate section as a result of the burst of diaphragm 1, the reflected rarefaction wave returning from the driver section, and the rarefaction wave resulting from the burst of the diaphragm 2 is very complex, the details of which are omitted from the figure. Finally, the shock wave traveling into driven section reflects from the enclosed right end to the tube, raising the pressure and temperature of the already shocked gas (state 7) to state 9.

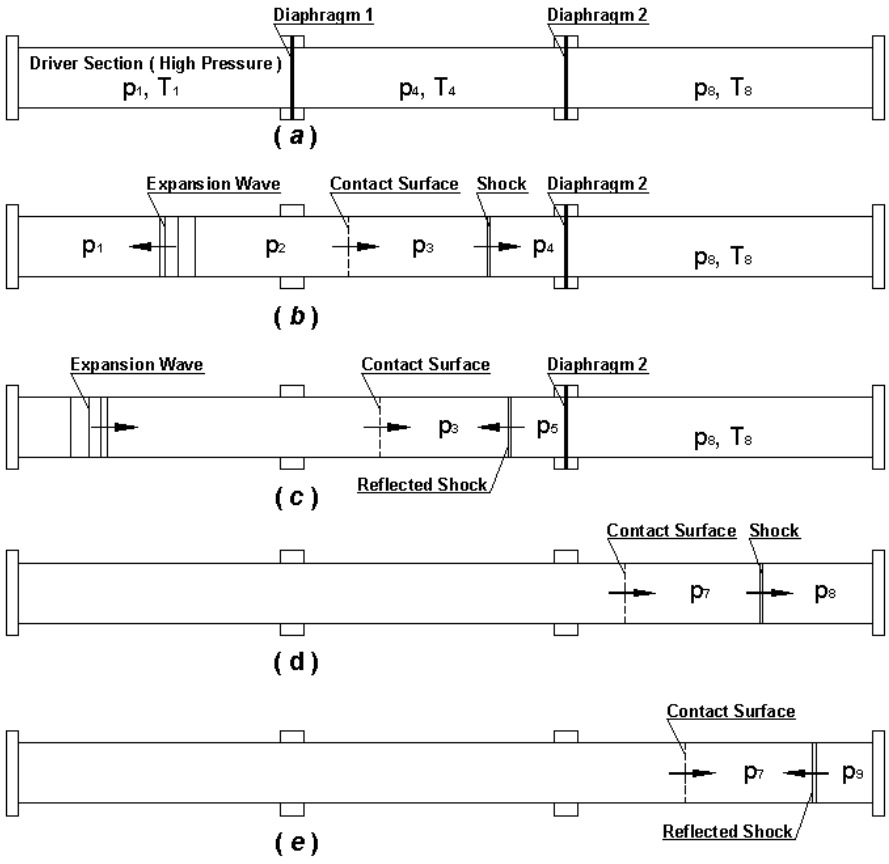

Figure 5. Motion of waves and gases in double diaphragm shock.

From the theory of shock tubes with a single diaphragm, the state of the fluid as it is approaching the second diaphragm is readily evaluated. If the state of the reflected gas (state 5)

is know, it can then be used as an input condition and the relevant equations can be applied across diaphragm 2, again according to the single diaphragm theory. The conditions state 5 are given below, without elaborating further on their development, in terms of the known conditions of state 4 (see Eq. (14)):

$$\frac{T_5}{T_4} = \frac{\left\{2(\gamma-1)M_4^2 + 3 - \gamma\right\}\left\{(3\gamma-1)M_4^2 - 2\gamma + 2\right\}}{(\gamma+1)^2 M_4^2}, \tag{15}$$

$$\frac{p_5}{p_4} = \left\{\frac{2\gamma M_4^2 - (\gamma-1)}{\gamma+1}\right\}\left\{\frac{(3\gamma-1)M_4^2 - 2\gamma + 2}{(\gamma-1)M_4^2 + 2}\right\}. \tag{16}$$

Shock Propagation in Shock Tubes with Conical Cross-Sections

When a normal shock wave passes through a uniform tube, the speed of the wave doesn't vary appreciably if frictional effects are negligible. This is no longer the case with tubes of varying cross sections. The differential equation, which relates change in the Mach number of the shock wave as it passes through a finite area change is given by Whitham [22] and is presented below. The governing differential equation is:

$$\frac{M}{M^2-1}\lambda(M)\frac{dM}{dx} + \frac{1}{A}\frac{dA}{dx} = 0. \tag{17}$$

In this relation, A is the cross sectional area of the tube as a function of distance (x). The variable $\lambda(M)$ is only a weak function of the Mach number and can be taken as being a constant, thus facilitating the solution, which can be written as:

$$\frac{M_2^2 - 1}{M_1^2 - 1} = \left(\frac{A_1}{A_2}\right)^{\left(\frac{2}{\lambda}\right)} \tag{18}$$

Real Shock Tube Behavior

The derivation of the above equations is based upon several assumptions that are enumerated in the remainder of the present paragraph. First, the properties of the gases are taken

as those described by Ideal gas conditions. Second, the shock tube is regarded as being adiabatic. Next, gas flow is considered to be initiated by the instantaneous removal of a plane diaphragm of negligible thickness. Also, viscosity and heat conductivity are regarded as not significant. Finally, the flow in the shock tube is taken as wholly unidirectional.

In reality, gases in the shock tube dissociate and ionize at high densities and temperatures. Also, heat does transfer to the surroundings through the shock tube wall. The first two of the above assumptions are not valid under these extreme conditions. Further, the bursting of diaphragm is generally not instantaneous. Also, experimental evidence suggests that the formation of shock wave takes place within a finite time period [23]. It is reported that at low values of driver to driven gas pressure ratio, plane shocks are observed, whereas higher pressure ratios give rise to shock waves that are semi-hemispherical near the diaphragm, gradually adopting a plane geometry with distance.

Finally, viscous forces are present and form a boundary layer on the walls of the tube and may affect the fluid flow. At high mach numbers, these viscous forces may even destroy the shock if the cross section of the tube is small enough. Therefore, the tube should be made neither too small nor too long, in order to conserve the integrity of the shock.

2.3 Design and Fabrication of the Shock Tube

The previous section describes in details the conditions existing within shock tubes that are totally enclosed. This configuration is generally used for cases where the trajectory of the flow within the tube is under investigation. The purpose of this study being one of evaluating the strength of materials that are not integral to the shock tube itself, the outlet of the driven section must therefore remain open to atmospheric conditions, and the material to be tested, placed near that location such as to experience the full burden of both the incoming and the reflected shocks.

The primary function of the design process of the shock tube is to arrive at a device that will expose the tested plates to as high a shock speed at as high a pressure as possible, within the size constraints impose by limited laboratory space. The process is undertaken by acquiring proper understanding of the physics associated with the equations described above, and applying them appropriately until an acceptable geometry is obtained. Two of the main considerations pertaining to that endeavor consist in taking advantage of the rises in pressure and velocity offered by the use of multiple diaphragms, and conical tube sections, respectively.

Recursive application of the relations presented in Section 2.3 lead to the choice of Helium, at room temperature, as the driver gas, and to a design that incorporates two diaphragms and convergent conical section preceding the exit of the driven section, as shown in Fig. 6.

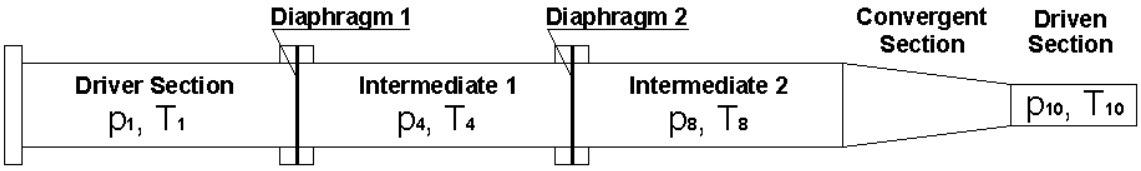

Figure 6. Schematic of double diaphragm shock tube with convergent section.

The shock tube material is Aluminum 6061 – T651 seamless [Tensile Yield Strength 40 ksi (276 MPa)]. The material is capable of handling a pressure in driver section of 2 ksi (17 MPa), with a safety factor of 3. The geometry of the various sections of the device is listed in Tbl. 1. The design is also modular, such that each section is separated into two, thereby allowing for the rearrangement to the device to suit different operating conditions.

Table 1.
Dimensions of the Shock Tube Sections

Name	Length (ft / m)	Length/Diameter
Driver Section	6 / 1.8	12
Intermediate Section 1	6 / 1.8	12
Intermediate Section 2	6 / 1.8	12
Convergent Section	2 / 0.6	5.3*
Driven Section	3 / 0.9	12

*Average diameter of conical section.

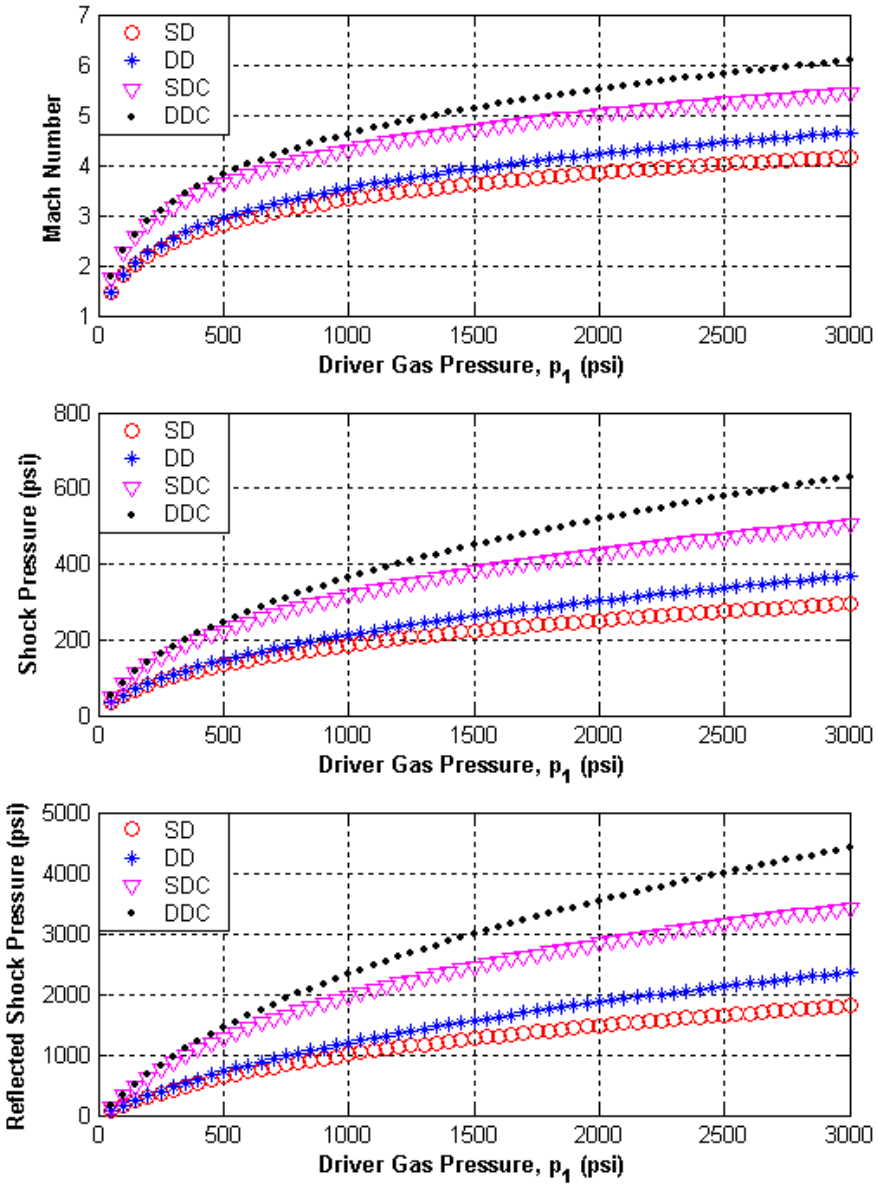

Figure 7. Comparison of different shock tube configurations. Legend: Single Diaphragm (SD), Double Diaphragm (DD), Single Diaphragm with Convergent section (SDC) and Double Diaphragm with Convergent section (DDC).

Figure 7 show variations in Mach number shock pressure and reflected pressure as a function of driver gas pressure. Note that these plots are unique to the current shock tube design when it is pressurized with helium. Based on the chosen safety factor of 3, the shock can attain a velocity corresponding to Mach 5.5, as well as shock and reflected pressures of 500 (3.4 MPa)

and 3500 psi (24 MPa), respectively. Further suggestions pertaining to the design of shock tubes can be found in Ref. [24] and [25].

Specifics of the Structural Design

One-eighth inch NPT threads (3.2 mm), 1.75 inches (44 mm) long, were machined on the outside diameter of the tubes, at both ends of each tube section. Aluminum flanges 1.5 inches (38 mm) wide mount the threaded sections of the tubes and opposite flanges are firmly connected by six, 1 inch (25 mm), steel bolts. One end of the driver section is sealed by an Aluminum plate of 1.5 inches thick. At one end of the mating tubes, two concentric grooves are machined to receive o-rings (see Figs. 8 and 9), except at the diaphragm locations (Fig. 10), where both mating ends have two o-ring grooves to provide a hermetic seal. The tubes are mounted on grooved aluminum plates that rest on steel frame standing on casters.

Figure 8. Driver section.

Figure 8 is a photograph of the driver section. Adjacent to the flange is the pressure transducer that measures the driver gas pressure. The closed end of the driver section receives

the gas inlet. Figure 9 faces one end of the Intermediate 1 section. At the other end, the muzzle of shock tube butts against the test plate (Fig. 11). The plate holding mechanism slides on guided rails and has the flexibility of providing diverse type of boundary conditions. The arrangement allows the plate to be moved in 3 perpendicular directions. The fully assembled shock tube is shown in Fig. 11.

Figure 9. Intermediate 1, Intermediate 2, Convergent, Driven section and dump tank.

Both aluminum and Mylar diaphragms were prepared, the latter being used for occurrences of relatively low pressure. To get different burst pressures, several Mylar diaphragms were compacted into one sheet, each set. Varying thicknesses of aluminum were used according to desired bursting pressure. These plates were scored to facilitate rupture.

Figure 10. Burst aluminum diaphragm.

Figure 11. Assembled Shock Tube.

Several sensors placed at varying locations along the shock tube monitor pressure variation and flow velocity. Results of repeated tests, show the shock tube generating a steady flow rate, thereby ensuring a constant fluid velocity within the smaller, driven section.

Figures 12 a), b), and c) show the deviation of the shock tube parameters compared to theoretical values. Within the range of the tests that were performed, Mach numbers under-estimate the predicted values by nearly 15%, whereas measured shock pressure values lag the theory by 30%. Measurements of the reflected pressures from the impacted plates, on the other hand, lag the theory by 60%. The latter discrepancy is due primarily to the fact that the impacted plates reside outside of the device, precluding return of the reflected gas within the tube, where the recording devices are positioned, prior to dissipation of the pressure into the atmosphere. Modifications are being considered, at present, to remedy these shortcomings.

a)

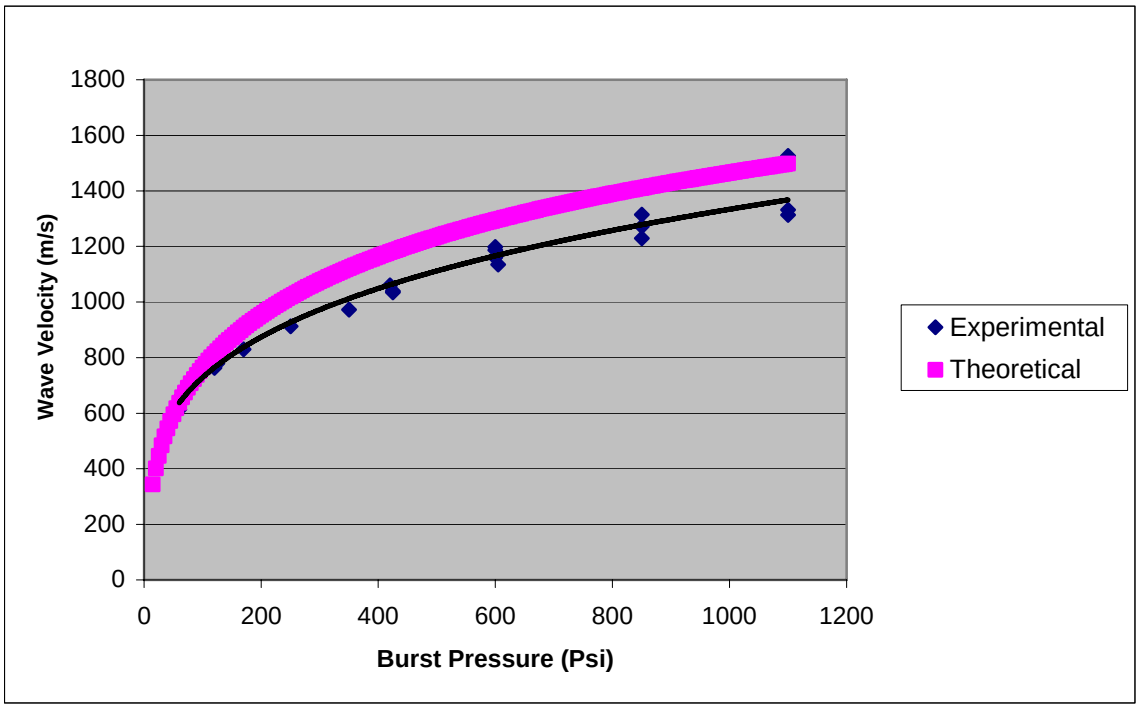
1800
1600
1400
1200
1000
800
600
400
200
0
Wave Velocity (m/s)
0
200
400
600
800
1000
1200
Burst Pressure (Psi)
Experimental
Theoretical

b)

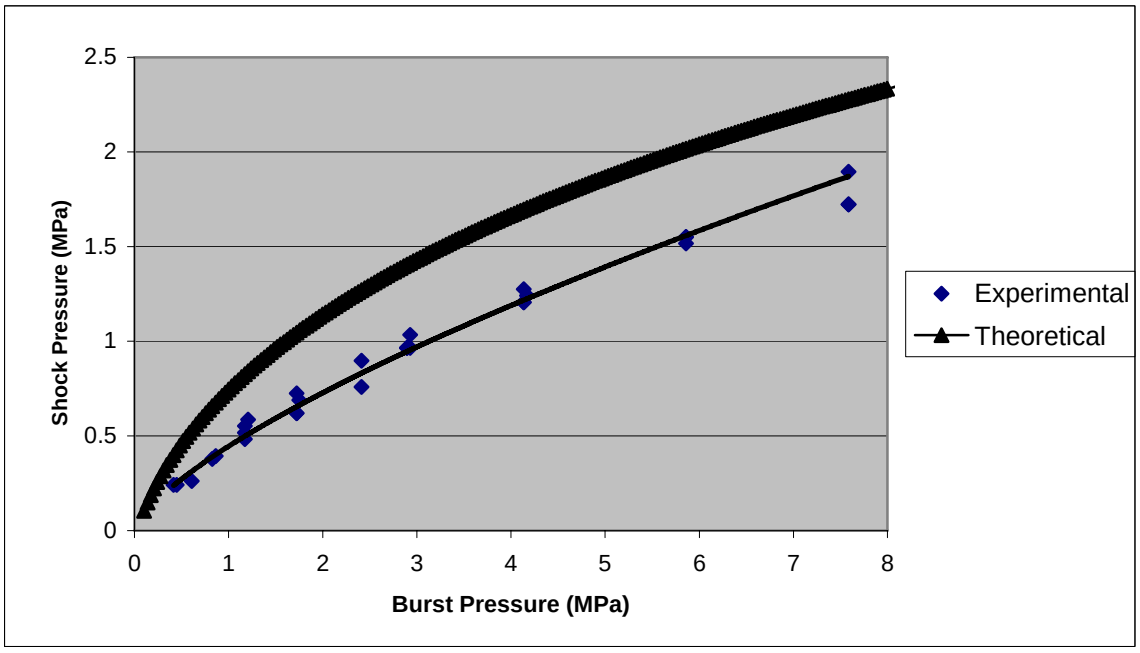
2.5
2
1.5
1
0.5
0
Shock Pressure (MPa)
0
1
2
3
4
5
6
7
8
Burst Pressure (MPa)
Experimental
Theoretical

c)

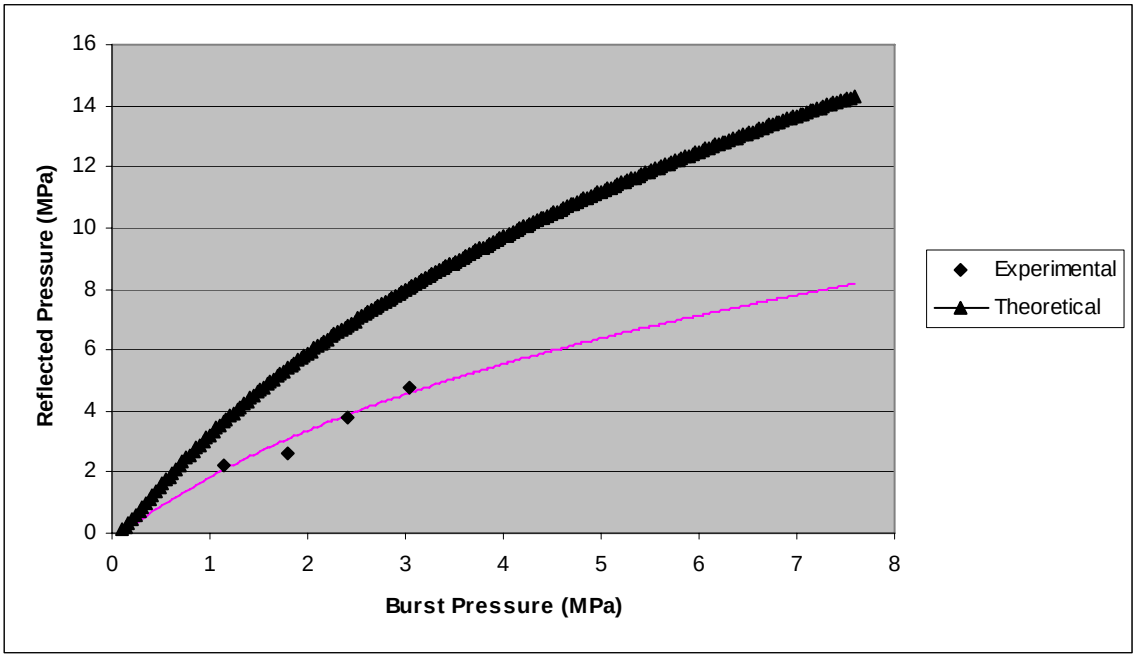

Figure 12. Variation of wave velocity (a), shock pressure (b), and reflected pressure (c) as a function of shock tube burst pressure.

3. DESIGN AND FABRICATION OF PROPOSED MATERIAL

The design and fabrication of composite materials was undertaken at 3TEX Inc. Composites are designed and fabricated from 3-D Woven S-2 Glass Fabrics and Dow Derakane 8084 Epoxy-Vinyl Ester resin. It is anticipated that these composites will have superior properties and structural integrity when subjected to blast loadings.

When designing 3-D weaves, the designers do not have a rigorous design criteria to determine all of the necessary weaving parameters and, particularly, to determine relative through thickness fiber content. However, certain semi-intuitive considerations can be applied. Among these the following three are primarily significant:

i. Fabric should be "balanced" in the weaver's sense, that is, there has to be close total amounts of reinforcement in the warp and fill directions. This is desirable in order to make the resulting composite "balanced" in a laminate sense, as its elastic and strength properties are as close as possible in the warp and fill directions.

ii. Resulting fabric and composite should have roughly square unit cells, of sizes close to the unit cell of 24oz plain weave "baseline" fabric (which is approximately 0.4" x 0.4" (10 mm)).

iii. Use around 3-4% of *Z* fiber volume content in resulting fabric (that would translate into 1.5- 2.0% of Z fiber volume fraction in resulting composite).

Due to the fact that there is always one fill layer more than warp layers, in order to satisfy requirement (i), a 3-D woven fabric must have either fewer yarns per inch in fill direction than in warp direction, or part of the yarns in fill direction shall be of a smaller size than the yarn used in warp direction.

The importance of requirement (iii) is explained as follows. The *Z* reinforcement, which is an immanent part of 3-D orthogonal weave, causes void pockets in the spatially separated layers of warp and fill reinforcements, thus reducing volume which could be otherwise occupied by fill (in the first place) and, at some extent, also by warp yarns and, accordingly, reducing the in-plane fiber volume fraction in resulting composite. Available experimental data and theoretical estimates indicate that the in-plane fiber volume fraction in 3-D weave composites

drops considerably when increasing *Z* fiber volume content in dry preform above 4-5%. On the other hand, it is believed that having at least 2-3% of *Z* fiber in dry preform is the minimum necessary to suppress delamination and sufficiently increase fracture resistance and damage tolerance of resulting 3 D weave composite. Thus, making preforms with 2-4% of *Z* fiber volume content would allow achieving the best possible trade off.

3TEX has designed fabrics using in house fabric geometry models (which relate weaving parameters to resulting fabric architecture) to areal weight, and "free state" preform thickness. Different aspects of such preform and composite design is illustrated for the case of “93oz” fabric (93 oz/yd^2 refers to areal weight of the fabric) in Figs. 13 through 16.

Figure 13. In-scale computer-generated images of “93oz” 3-D woven fabric (left) and its composite (right) elements.

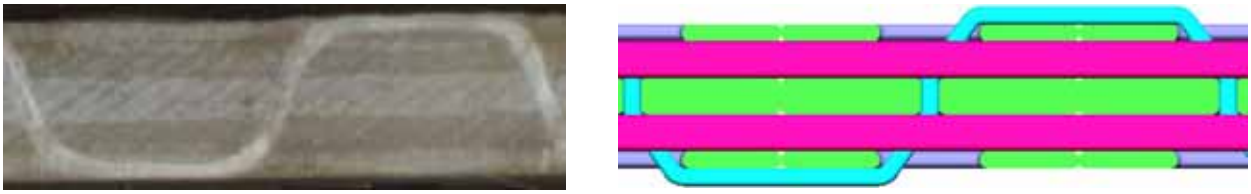

Figure 14. Experimental (left) and computer-generated (right) cross-sectional images of "93oz" 3-D woven fabric composite.

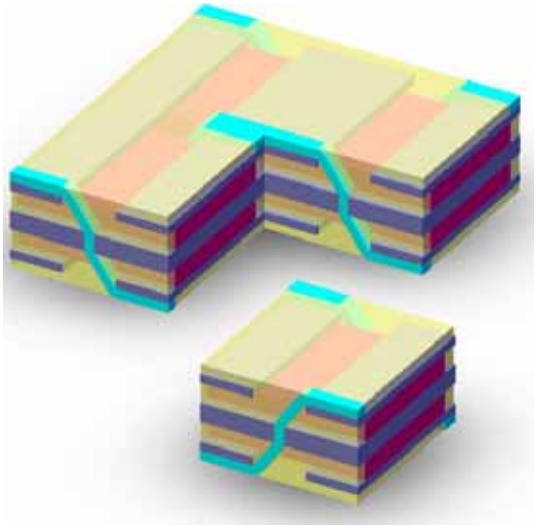

Figure 15. Unit Cell construction of "93oz" 3-D woven fabric composite.

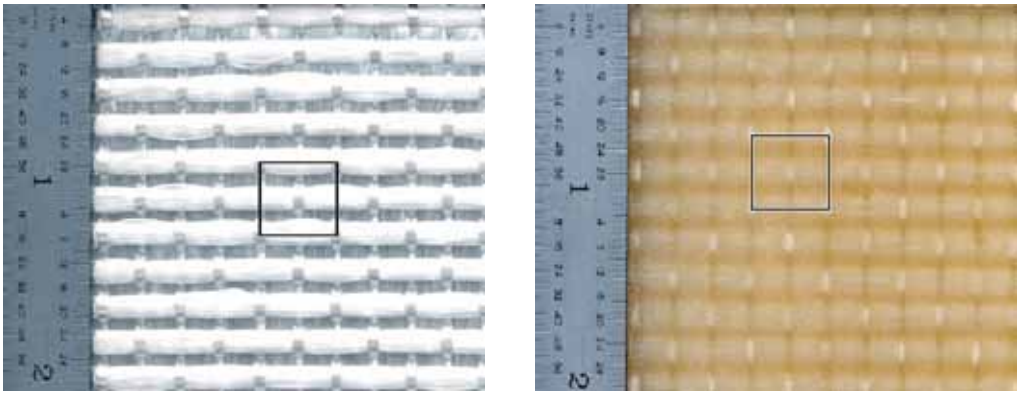

Figure 16. Surface photos of "93oz" 3-D woven fabric (left) and its composite (right).

4. VERIFICATION OF THE NUMERICAL SCHEME

4.1 Introduction

The numerical scope of the project, in the first year, was to develop a numerical model with the capability of simulating the experiments. This effort was spearheaded by the 3TEX, Inc. The formulation and set-up of the numerical code was successfully conducted, and is presented below, following a brief survey of existing blast modeling techniques.

There is a large bulk of literature on explosives, explosions, blast wave formation and propagation, dynamic blast loads, structural response, and other related topics (see for example reference books [26 - 28] and other useful literature [29 - 32]). Typical structural materials are highly vulnerable to blast overpressure even if exposed to low-mass explosive charges at relatively short standoff distances. Predecessors of total fracture and collapse of the structures exposed to blast overpressure are initiation and growth of cracks, their coalescence, followed by the material fragmentation, and spalling from the back surface. All of these phenomena occur in a very short (milliseconds) time range. There are many analytical and computational approaches

aimed at this class of theoretical problems, ranging from quite simplistic closed-form solutions to 3-D dynamic finite element package LS DYNA. One finite element analysis approach, which is relatively simplistic [29], is often used in blast response analysis of civil engineering structures. It assumes that each building component responds as the equivalent single-degree-of-freedom system. This approach was recommended in some of the blast resistant structures design manuals [33, 34].

Design and optimization of blast mitigation barriers aimed at protecting various structures and transportation systems vulnerable to the terrorist attacks require extensive theoretical studies. These should address a number of specific research problems (discussed, for example, in references [29 - 32]), including establishing relations between the "ideal" or "non-ideal" (such as ANFO) explosive characteristics on one side and the "field-free" blast pressure history on the other. Importantly, the true, so-called "reflected blast pressure" acting on the front wall may significantly exceed the peak field-free pressure.

A blast pressure history is typically characterized by the peak pulse pressure and pulse duration. It is commonly assumed in a simplistic (though often used) analysis assumption that the blast pressure rises instantaneously to its peak value. In the computational problem to be analyzed here, a more general consideration is taken, i.e., the pressure rises to its peak value during some very short time period (typically several microseconds), and then decays (relatively slowly) to ambient (or even negative) pressure. A typical pulse shape is shown in Fig. 17.

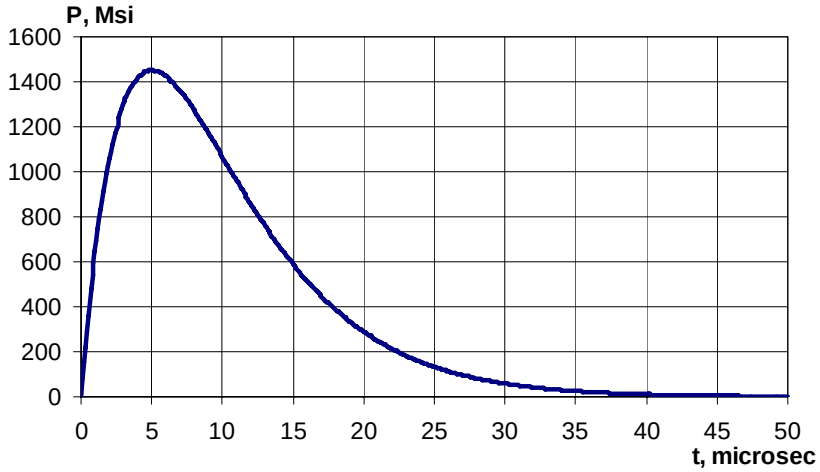

Figure 17. A typical Pressure-Time variation associated with an incident blast pulse. The pulse peak value and its duration are taken arbitrarily here; for any specific blast loading case they have to be related to the explosive characteristics.

The applications of 3-D Mosaic model and variational analysis approach developed in [33 - 35] has been demonstrated by Bogdanovich and Yushanov [36 - 37] for some typical blast loading problems, one of which [37], made of 3-D woven composite skins and Balsa core, is briefly discussed here. A detailed numerical analysis of that problem is illustrated by the time variations of displacements and stresses, with special emphasis on the criteria for computational accuracy evaluation.

4.2. Formulation of Boundary Conditions

In this section the basic for numerical simulations of 3-D dynamic boundary value problems is presented. The numerical code specifically models multi-layer flat square panels that are exposed to uniformly distributed blast pressure pulses. The panel schematic, boundary conditions and load distribution are illustrated in Fig. 18. The transverse (z-directional) displacement, u_z, is assumed to be zero along all four sides of the panel.

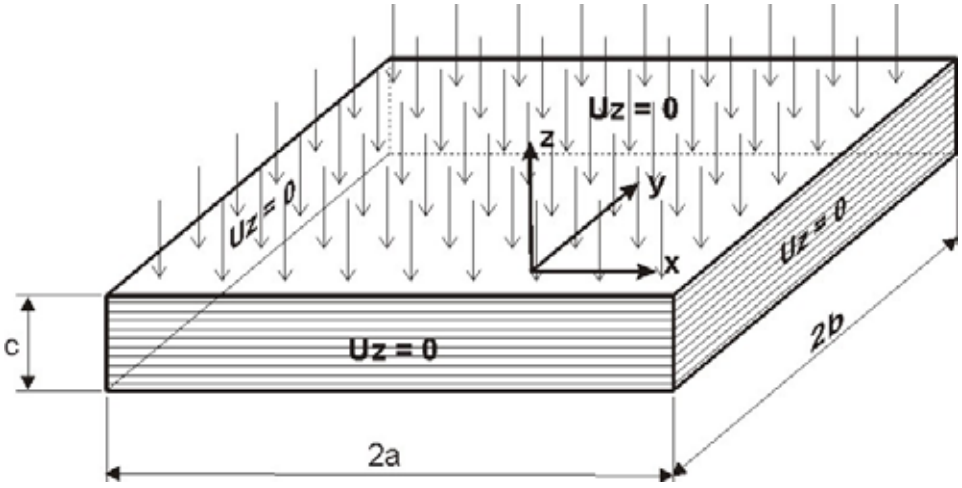

Figure 18. Schematic of a multi-layer panel exposed to uniformly distributed pressure pulse, and boundary conditions imposed along the side surfaces.

Due to an obvious symmetry of the boundary value problem under consideration, the ¼th section of the panel shown in Fig. 19 can be solved in place of the whole panel of Fig. 18. In this case, the symmetry boundary conditions $u_x = 0$ at the left surface $x = 0$ and u_y at the front surface $y = 0$ shall be added. Still, the boundary condition $u_z = 0$ remains imposed on the right surface $x = a$ and on back surface $y = b$.

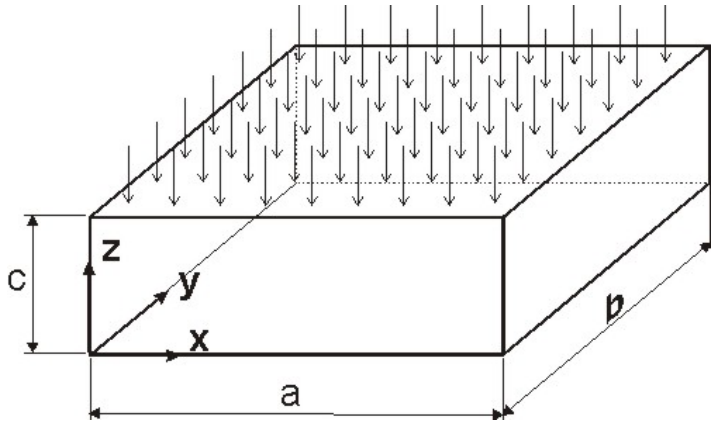

Figure 19. One-quarter of the panel solved in present analysis.

4.3. Verification of Computational Meshes

It is important to note that a comprehensive convergence study has been performed as part of this analysis in order to select the computational mesh, which assures that the obtained results are sufficiently accurate. That analysis is omitted here in favor of the presentation of numerical results obtained for some specific computational meshes described below.

The computational mesh is shown in Fig. 20 for a sandwiched composite of which the outer layers are made of three-dimensionally woven material. Two intervals are used in each of the x and y directions; one of them is twice as large as the other. Computational meshes used for the individual layers in through thickness (z-direction) are very fine and nonuniform: each layer is symmetrically discretized into 10 intervals, 5 of them in the upper half of the layer and another 5 in the lower half. Within half-thickness of a layer, the z-directional discretization mesh is non-uniform, where the largest interval is adjacent to the mid-surface of the layer, and each next (moving towards the outer surface) interval is four times smaller. So, the ratio of the largest to smallest interval within the layer is 256. This high mesh non-uniformity allows one to increase accuracy of results near the interfaces between distinct layers, as well as near the panel facings (one of them is loaded, while the other one is free). Third degree Bernstein polynomials are utilized for all three coordinate directions x, y and z.

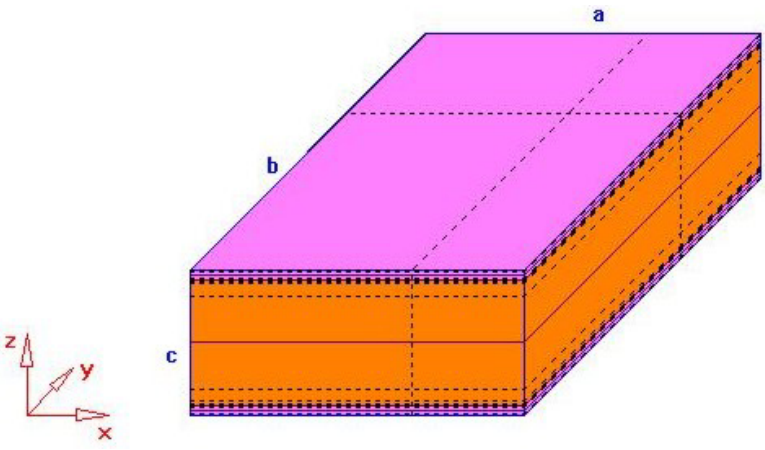

Figure 20. Discretization mesh.

In order to illustrate the accuracy of the performed analysis, the following control characteristics have been chosen:

(i) The incident pulse shape $P(t)$ (which is one of input parameters for the analysis) is compared with the computed time variation of the transverse normal stress component $\sigma_z(t)$ at the upper (loaded) surface of the panel. Clearly, an exact solution would yield $P(t) = \sigma_z(t)$ at any instant in time. Therefore, the discrepancy between two sides of this equality can be used as the numerical solution accuracy criterion. Such accuracy control has been performed for the center point of the panel ($x = 0, y = 0$) in each analysis case.

(ii) Time functions $\sigma_z^-(t)$ from the bottom and $\sigma_z^+(t)$, from the top of each interface between distinct material layers, are compared. The exact solution these two values would yield $\sigma_z^-(t) = \sigma_z^+(t)$ at any instant in time. Hence, the discrepancy between two sides of this equation can be also used for the numerical solution accuracy control. This accuracy control criterion is also applied at the center point of the panel ($x = 0, y = 0$).

Numerical results for the simulated panel are presented in Fig. 21. Figure 21(a) shows a comparison between the incident pulse $P(t)$ and computed stress response $\sigma_z(t)$ on the loaded surface $z = c$ at the center of the panel. It is seen that there is a small difference near the peak, otherwise the two curves are practically identical. The observed difference can be reduced to any small value by refining the computational mesh (particularly, using more intervals for the upper skin in z-direction).

Fig. 21(b) shows a comparison of $\sigma_z^-(t)$ and $\sigma_z^+(t)$ computed respectively from the bottom and from the top at the upper interface. The two curves are barely distinguishable, which is an important indication of the accuracy of the analysis performed.

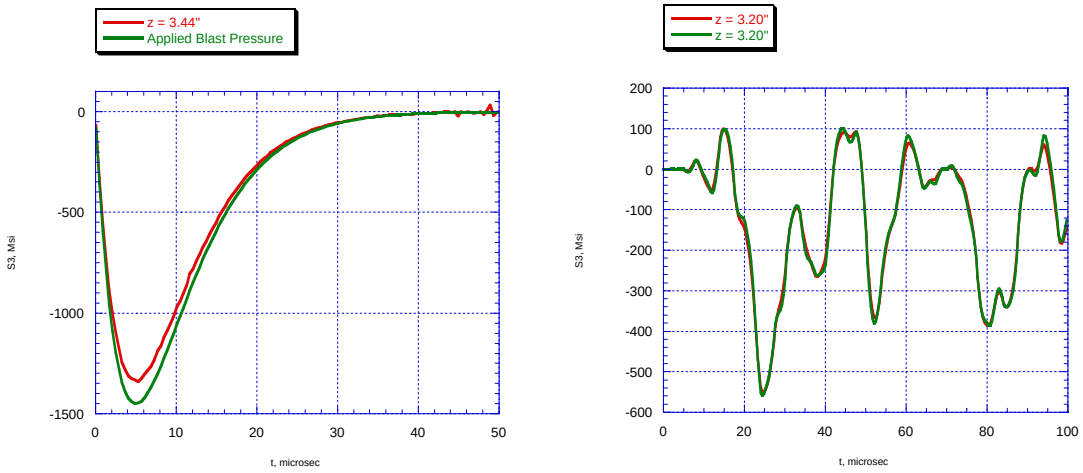

Figure 21. Numerical results for Panel #1.

These results show the adequacy of the numerical model used for this sandwich composite. Note that for the outer layers, the following material properties are used:

$$E_1 = 26.46\ GPa,$$
$$E_2 = 26.74\ GPa,$$
$$E_3 = 12.45\ GPa,$$
$$G_{12} = 3.48\ GPa,$$
$$G_{13} = 3.32\ GPa,$$
$$G_{23} = 3.33\ GPa,$$
$$\nu_{12} = 0.11,$$
$$\nu_{13} = 0.34,$$
$$\nu_{213} = 0.34.$$

These values are the properties of a 98 oz. 3-D Weave, where the index 1 corresponds to warp direction; index 2 corresponds to the fill direction; and index 3 corresponds to the *Z* or out-of-plane fiber direction.

The robustness of the model having been established, it will be used in the second year of this project to try and duplicate the experimental results. Calibration of the model will be undertaken by comparing such parameters as wave propagation speed and surface strain data with the experiments. Other parameters that cannot be obtained experimentally, such as inner stress states of the material, can then be extracted numerically.

5. BLAST LOADING EXPERIMENTS

5.1 Materials Available for Testing

3TEX, Inc. has prepared several specimens that were submitted for testing under impulsive conditions. All panels are 12" x 12" (0.3 m). As described in a previous section, the panels were manufactured using vacuum assisted resin transfer molding, with the fibers woven from S-2 glass. Following air curing, the panels were maintained at 180^{o} F for 16 hours. A list of available specimens with their respective configurations is listed in Tbl. 2. A typical specimen within its enclosing frame is shown in Fig. 22. The exposed area is 9" x 9" (0.22 m).

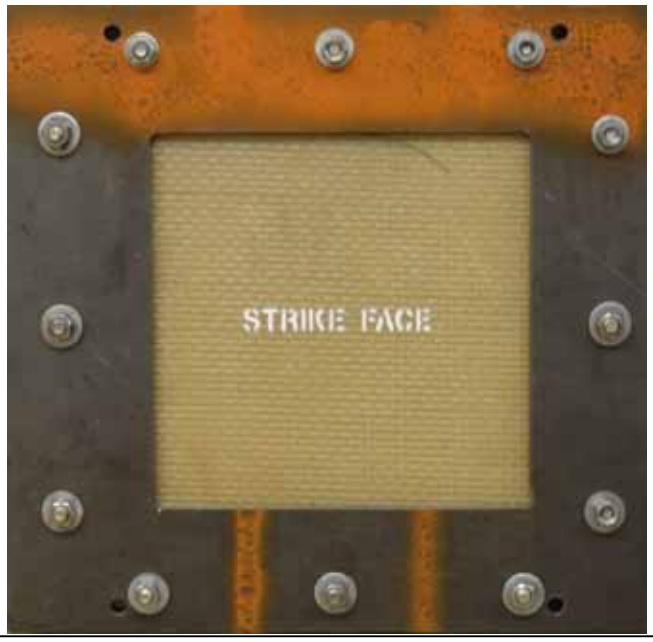

Figure 22. Photograph of specimen prior to testing.

Table 2.
3D Weave materials procured for testing.

Designation	Weight (g)	Min thickness (mm)	Max thickness (mm)
Single Ply			
93	436	2.7	2.9
98	452	2.8	3.0
100	446	2.9	3.1
190*	899	5.7	6.0
190*	915	5.8	6.1
190*	875	5.3	5.7
190	893	5.8	5.9
190	839	5.2	5.7
190	840	5.3	5.5
190	855	5.4	5.5
190	875	5.6	5.7
190	869	5.6	6.0
Double Ply			
93*	900	5.8	6.0
93*	895	5.6	5.9
93*	873	5.3	5.8
93	839	5.3	5.7
93	842	5.6	5.9
93	839	5.6	5.7
93	835	5.3	5.8
93	865	5.6	5.9
98*	940	6.0	6.6
98*	1008	6.7	7.0
98*	959	6.3	6.7
98	925	5.7	6.0
100	866	5.6	5.8
100	854	5.3	5.7
100	841	5.2	5.7
100	852	5.3	5.6
100	859	5.3	5.7

* First batch of material provided in March 2004 (remainder received in October 2004).

The cross-sections of a typical single ply panel was shown in Fig. 14. Weaving in the out-of-plane direction can be seen clearly. Double ply panels are made of superimposed single ply panels bonded solely with epoxy. The cross-section of the former is shown in Fig. 23

Figure 23. Double-ply cut-out.

5.2 Experiments

Experiments were conducted using the shock tube, as described in Section 2. The panels were placed a few millimeters from the exit of the shock tube, such as to receive the full effect of the blast at its center, over a diameter of 3 inches (76 mm). In addition, the close proximity of the plate allow for reentry of the reflected wave into the shock tube, where the level of the reflected shock can be measured. The veracity of this assertion was determined by placing a steel plate with a central threaded hole in the loading mechanism. Measurements were then taken simultaneously by a transducer threaded into the plate and by the transducer that permanently resides in the shock tube. The pressure records were identical.

The test panels were outfitted with strain gages located on their back sides. They were typically placed perpendicularly to each other, say along the 0^o and the 90^o axes of the plane. In addition, along each axis, at least two strain gages were positioned in order to monitor the radial speed and evolution of the traveling waves.

The panels were initially tested at low input pressures that were gradually increased. However, once subjected to an initial blast, a panel was not reused, regardless of its apparent condition. Instead, they were sectioned into numerous specimens that underwent microscopic examination, and survey for possible fiber or matrix damage. The lowest input pressure in the driver section of the shock tube was 175 psi (1.2 MPa), which corresponds to a shock pressure of

80 psi (0.5 MPa), a reflected pressure of 200 psi (1.4 MPa), a shock speed of 925 m/s, or Mach 2.4. At that level, no damage was detected. Further increases resulted in superficial damage, evident by slight discoloration of the fibers (Fig. 24), particularly at the corners. The maximum input pressure achieved was 850 psi (5.8 MPa), at which point permanent plate deformation occurred.

Figure 24. Surface damage to plate subjected to 600 psi input pressure.

Figure 25. Extensive fiber damage in plate subjected to 850 psi input pressure.

As can seen in Fig. 25, the damage for a shock tube input pressure is no longer solely superficial, but displays severe fiber damage and delamination particularly along the clamped edges. Associated with such damage, in the case of other plates, is severe bowing of the panel by more than 50 mm. Specimens taken from these panels will later undergo microscopic scrutiny of visual evaluation of internal damage, compressive testing for examination of their residual strength.

5.3 Post-Mortem Evaluation

Following shock tube testing the panels were subjected to further experimental burden, to better understand the effect of the applied impulse. Residual compressive strength were performed with the aid of a device built specifically for that purpose during the course of the project. It is shown in Fig. 26, and is designed to receive slender, elongated specimens. Results of compression tests performed on specimens subjected to pressure within the lower pressure ranges are listed in Tbl. 3.

Figure 26. Compression apparatus.

It is first noted that the virgin specimen tend to have increasing strength with increasing weight. The 190 oz specimen, on the other hand, does see its strength taper down. This is due to the fact that a single ply panels of lower designation have a lower per ply thickness. Therefore, the out-of-plane woven fiber have a lesser propensity for buckling. The compressive tests show an overall tendency of material weakening with increasing shock tube burst pressure. However,

the 93 oz panel does display a counter-trend, whereby increasing loading actually toughens the material. This phenomenon is not as of yet understood.

Table 3.
Result of compressive testing.

Panel Designation[1] (oz)	Burst Pressure (psi/MPa)	Compressive Strength[2] (MPa)	Compressive Strength[3] (MPa)
93	0	253	336
93	250 / 1.7	265	307
93	425 / 2.9	281	322
98	0	295	330
98	600 / 4.1	230	284
190	0	272	242
190	425 / 2.9	231	-
190	600 / 4.1	228	260

[1] All specimens are double-plies except for the 190 oz.
[2] Weft direction.
[3] Wart direction.

The compression tests show to main types of failure, mainly, fiber crushing (Fig. 27(a)) and fiber kinking (Fig. 27(b)). Enlarged pictures of the same are shown in Fig. 28. The more heavily weighted, single-ply 190 oz specimens are more prone to fiber crushing, whereas the lighter weighted, double-ply specimens favor the kinking failure mode.

Figure 27. Two forms of failures obtained during compression testing: a) fiber crushing (190 oz) and b) fiber kinking (93 oz).

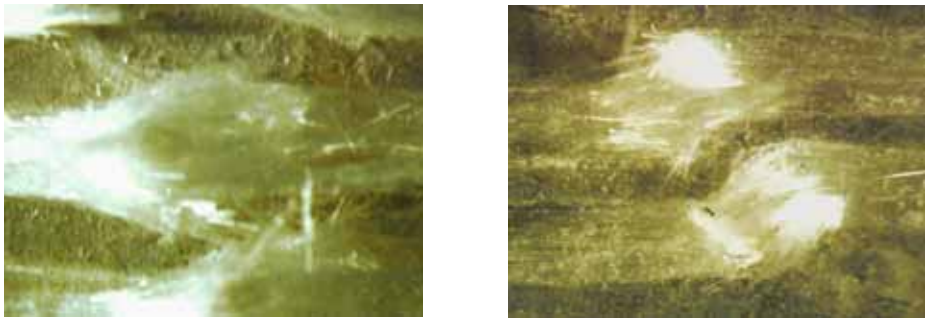

Figure 28. Microscopic examination of a) crushed and b) kinked fibers.

6. SUMMARY

The project achieved its main objective, that of establishing a shock loading facility at the University of Rhode Island. This challenging task was very labor intensive and required enlisting effort from several graduate, undergraduate students, as well as university staff and local machinists. The designed shock tube is capable of producing blasts in excess of the energy output of black powder. In addition, the relative performance of three-dimensional panels from 3TEX, Inc. was initiated. Post-mortem evaluations performed on those panels indicate that the use of superimposed lighter weight plies is preferable to using heavy weight multiple plies, and by far exceeds the performance of heavy single plies of the same thickness. Further evaluation of the 3D weave material will continue during the second stage of the project, with its performance measured against panels currently in use in transportation, to establish its viability for use in that industry to mitigate the effects of blast loading. The numerical effort will also continue and will focus on the duplication of specific experimental parameters.

7. ACKNOWLEDGEMENT

The authors would like to acknowledge support from the Transportation Center at the University of Rhode Island under Grant 500230400000000057-2003. Additional support was also provided by 3TEX, Inc. of Cary North Carolina.

REFERENCES

[1] S. Chung Kim Yuen and G. N. Nurick, "Experimental and numerical studies on the response pf quadrangular stiffened plates. Part I: subjected to uniform blast load.," in *International Journal of Impact Engineering*, vol. 31, issue 1, pp. 55 – 83, 2005.

[2] G. S. Langdon, S. Chung Kim Yuen and G. N. Nurick, "Experimental and numerical studies on the response pf quadrangular stiffened plates. Part II: localized blast load.," in *International Journal of Impact Engineering*, vol. 31, issue 1, pp. 85 – 111, 2005.

[3] H. S. Turkmen and Z. Mecitoglu, "Dynamic response of a stiffened laminated composite plate subjected to blast load.," in *Journal of Sound and Vibration*, vol. 221, issue 3, pp. 371 – 389, 1999.

[4] T. Wierzbicki and A. L. Florence, "A theoretical and experimental investigation of impulsive loaded clamped circular viscoelastic plates.," in *International Journal of Solids and Structures*, vol. 6, issue 5, pp. 553 – 568, 1970.

[5] A. L. Florence, "Circular plate under a uniformly distributed impulse.," in *International Journal of Solids and Structures*, vol. 2, issue 1, pp. 37 – 40, 1966.

[6] Abel Carlos Jacinto,Ricardo Daniel Ambrosini and Rodolfo Francisco Danesi, "Experimental and computational analysis of plates under air blast loading.," in *International Journal of Impact Engineering*, vol. 25, issue 10, pp. 927 – 947, 2001.

[7] A. L. Florence and R. D. Firth, "Rigid-plastic beams under uniformly distributed impulses.," in *Transactions of ASME , Journal of Applied Mechanics*, vol. 32, series E, number 3, pp. 481 – 488, Sept. 1965.

[8] M. V. Dharaneepathy, M. N. Keshava Rao and A. R. Santhakumar, "Critical distance for explosive blast-resistant design.," in *Computers and Structures*, vol. 54, No. 4, pp. 587 – 595, 1995.

[9] A. P. Mouritz, "The effect of underwater explosion shock loading on the flexural properties of GRP laminates.," in *International Journal of Impact Engineering*, vol. 18, No. 2, pp. 129 – 139, 1996.

[10] Walker Bleakney, D. K. Weimer and C. H. Fletcher, "The Shock Tube: A Facility for investigations in Fluid Dynamics.," in *The Review of Scientific Instruments*, vol. 20, No. 11, pp. 807 – 815, Nov. 1949.

[11] J. K. Wright, *Shock Tubes*. Methuen and Co. Ltd. London, 1961.

[12] E. H. Andrews, L. Bernstein, P. J. Nurse, and P. E. Reed, "Impact testing of plastics using a shock tube.," in *Proceedings of 8th International Shock Tube Symposium*, (Imperial College, London), pp. 60/1 – 60/12, Jul. 1971.

[13] J. L. Stollery, A. G. Gaydon and P. R. Owen, "Shock produced strain relaxation in aluminum.," in *Proceedings of 8th International Shock Tube Symposium,* Imperial College, London, pp. 59/1 – 59/9, Jul. 1971.

[14] Joseph M. Santiago, "Plate response analysis using a shock tube.," in *Proceedings of 16th International Symposium on Shock Tubes and Waves ,* Aachen, West Germany, pp. 935 – 941, Jul. 1987.

[15] L. H.Hernandez-Gomez and C. Ruiz, "Assessment of data for dynamic crack initiation under shock pressure loading; Part I–Experiment.," in *Theoretical and Applied Fracture Mechanics*, vol. 19, issue 1, pp. 75 – 83, Jun.1993.

[16] Francois Toutlemonde, Pierre Rossi, Claude Boulay, Christian Gourraun, Dominique Guedon, "Dynamic behaviour of concrete: tests of slabs with a shock tube.," in *Materials and Structures*, vol. 28, pp. 293 – 298, 1995.

[17] M. Stoffel, R. Schmidt and D. Weichert, "Shock wave-loaded plates.," in *International Journal of Solids and Structures*, vol. 38, issues 42 – 43, pp. 7659 – 7680, Oct. 2001.

[18] Chr. Mayrhofer, "Reinforced masonry walls under blast loading.," in *International Journal of Mechanical Sciences*, vol. 44, issue 6, pp. 1067 – 1080, Jun. 2002.

[19] John D. Anderson, Jr., *Fundamentals of Aerodynamics*. McGraw-Hill International Edition, 3e, Singapore, 2001.

[20] Bacue, R. H., "The Double Diaphragm Shock Tube." MS Thesis, New Mexico State University, New Mexico, May 1973.

[21] B. D. Henshall, "The Use of Multiple Diaphragms in Shock Tubes.," in *Aeronautical Research Council Technical Report*, C.P.No.291(18062), London, 1956.

[22] G. B. Whitham, *Linear and Nonlinear Waves*. John Wiley & Sons, New York, 1974.

[23] J. Lukasiewicz, "Shock Tube Theory and Applications.," in *National Aeronautical Establishment*, Report 15, Canada, 1952.

[24] Warren, W. R., Harris, C. J., "A Critique of High Performance Shock Tube Driving Techniques.," in *Proceedings of the Seventh International Symposium* held at University of Toronto, Canada, pp. 143 – 176, 23 – 25 Jun. 1969.

[25] Glass, I. I., "Shock Tubes: Part I: Theory and Performance of Simple Shock Tubes.," in University of Toronto Institute of Aerospace Studies (UTIAS) Review No. 12, Toronto, Canada. May 1958.

[26] Baker, W. E., Cox, P. A., Westine, P. S., Kulesz, J. J., and Strehlow, R. A., Explosion Hazards and Evaluation, Elsevier Scientific, New York, 1983.

[27] Kinney, G.F. and Graham, K. J., Explosive Shocks in Air, Springer-Verlag, New York, 1985.

[28] Zukas, J. A. and Walters, W. P., Explosive Effects and Applications, Springer, New York, 1998.

[29] "Structures to Resist the Effects of Accidental Explosions," Technical Manual for Army TM 5-1300, Navy NAVFAC P-397, and Air Force AFR 88-22, November 1990.

[30] "Design of Blast Resistant Buildings in Petrochemical Facilities," prepared by the Task Committee on Blast Resistant Design of the Petrochemical Committee of the Energy Division of the ASCE, 1997.

[31] "Design and Analysis of Hardened Structures to Conventional Weapons Effects," Technical Manual for Army, TM 5-855-1, Air Force AFPAM 32-1147(I), Navy NAVFAC P-1080, and Defense Special Weapons Agency DAHSCWEMAN-97, August 1998.

[32] Wesevich, J.W. and Abernathy, R.L., "Inelastic Structural Component Response Comparisons Between ANFO and TNT Based on Recent Air Blast Data at Scaled Ranges of 1.4 to 68 ft/lb$^{1/3}$," presented at International Workshop on the Modeling of Non-Ideal Explosives, Socorro, New Mexico, March 16-18, 1999.

[33] A. E. Bogdanovich, "Three-Dimensional Variational Theory of Laminated Composite Plates and Its Implementation with Bernstein Basis Functions", Computer Methods in Applied Mechanics and Engineering, 2000, Vol. 185, No. 2-4, pp. 279-304.

[34] A. E. Bogdanovich and S. P. Yushanov, "Three-Dimensional Variational Impact Contact Analysis of Composite Bars and Plates", Composites Part A: Applied Science and Manufacturing, 2000, Vol. 31A, No. 8, pp. 795-814.

[35] Bogdanovich, A. E., "Multiscale Predictive Analysis of 3-D Woven Composites," Proceedings of 35th International SAMPE Technical Conference, Vol. 35, Dayton, OH, September 28-October 2, 2003.

[36] Bogdanovich, A. E. and Yushanov, S. P. "3-D Blast Performance Analysis of Concrete Walls with Layered Composite Protection/Retrofit", Proceedings of The American Society for Composites, Fourteenth Technical Conference, September 1999, Dayton, OH, pp. 151-160.

[37] Bogdanovich, A. E. "3-D Modeling of Stress Wave Propagation and Blast Effects in Composite Sandwich Structures", SBIR Report, submitted to U.S. Navy by 3TEX, Inc., 2004.